Supplementary Information for

Centimeter-Long Weavable Fibers of Carbon Nanotubes with Giant Thermoelectric Power Factor

Natsumi Komatsu[1], Yota Ichinose[2], Oliver S. Dewey[3], Lauren W. Taylor[3], Mitchell A. Trafford[3], Yohei Yomogida[2], Geoff Wehmeyer[4,5], Matteo Pasquali[3,5,6,7], Kazuhiro Yanagi[2], Junichiro Kono[1,7,8,]*

[1] Department of Electrical and Computer Engineering, Rice University, Houston, Texas, USA

[2] Department of Physics, Tokyo Metropolitan University, Tokyo, Japan

[3] Department of Chemical and Biomolecular Engineering, Rice University, Houston, Texas, USA

[4] Department of Mechanical Engineering, Rice University, Houston, Texas, USA

[5] Carbon Hub, Rice University, Houston, Texas, USA

[6] Department of Chemistry, Rice University, Houston, Texas, USA

[7] Department of Materials Science and NanoEngineering, Rice University, Houston, Texas, USA

[8] Department of Physics and Astronomy, Rice University, Houston, Texas, USA

*Corresponding author. Email: kono@rice.edu

Estimation of the position of E_F by optical spectroscopy studies

Thin films of aligned CNT were produced by a facile blade coating technique [1]. The raw CNT material was dissolved in CSA at a concentration of 0.5 wt%. The solution was pipetted onto a glass microscope slide and pressed between another slide to fully coat both slides. The slides sandwiched with solution were put into a custom-built poly(tetrafluoroethylene) (PTFE) holder. A PTFE push stick was used to quickly shear (at a rate of $\sim 10^4$ s^{-1}) the two glass sides apart from each other. This shearing force induced a uniaxial alignment of the CNTs. The films were then coagulated into acetone to remove the CSA and stabilize the aligned films.

The absorption spectra of CNT films were measured by a home-built optical measurement setup, consisting of a tungsten-halogen lamp (SLS201L, Thorlabs), a Glan-Thompson polarizer, and two spectrometers (covering 550-1080 nm and 1080-1425 nm). The spectral range of 1425-3300 nm was measured by Fourier transform infrared spectrometer (Nicolet™ iS50 FTIR Spectrometer, Thermo Fisher Scientific). The beam size was ~1 mm. Figure S8 shows absorbance spectrum of the film for both cases where the incident light polarization direction and CNT alignment directions were parallel and perpendicular to each other.

For solution samples (Figure S7), the raw CNT material was dispersed in water using sodium deoxycholate (Sigma-Aldrich). UV-VIS spectrophotometer (UV-1800, Shimadzu) was used for the spectrum range of 300-1080 nm, and the home-built setup was used for 1080-1300 nm.

Optical spectroscopy provides information on the nanotube diameter distribution and the position of E_F in each CNT sample; the latter is particularly important since the *S* value strongly depends on E_F from Ref. [2,3]. Figure S7 shows an absorbance spectrum for an aqueous suspension of the raw CNT material. The chiralities of the inner-wall nanotubes were assigned based on information available in the literature [2,3]. The diameters expected for the inner-wall nanotubes from Figure S7 agree with results of our TEM analysis and are summarized in the top graph of Figure S8a.

Figure S8a compares expected absorbance peak positions based on the diameter distribution determined by the TEM analysis with absorbance spectra of the four films that underwent the same chemical treatments as the four fibers in the TE measurements. Diameter information allows us to determine absorbance peaks originating from excitonic optical transitions [2,3], as shown in the top figure of Figure S8a. Absorption peaks originating from the outer semiconducting tubes (S_{11} and S_{22}) are highlighted in red, those from the inner semiconducting tubes are highlighted in blue, and those from both the outer and inner metallic tubes (M_{11}) are in green.

The annealed films (annealed at 350 ˚C and 500 ˚C, respectively) show a peak at around 0.57 eV due to the S_{11} transition of the outer CNTs. A band of absorption peaks observed from 0.8 to 1.2 eV are due to a combination of the S_{22} peaks of the outer CNTs and the S_{11} peaks of the inner CNTs. Peaks are red-shifted compared to SWCNTs in an aqueous sodium dodecyl sulfate suspension (the top figure) [2,3]. The intensity of the S_{11} absorption band of the outer CNTs is lower than that of the S_{22} absorption band of the outer CNTs, suggesting that E_F is likely to be inside the valence band, rather than inside the bandgap. Absorbance spectra for the

as-produced and ICl-doped films are drastically different from those for the annealed ones, with the S_{11} and S_{22} peaks of the outer CNTs being suppressed due to Pauli blocking. The S_{11} peaks of the inner CNTs are still visible (from 1.0 to 1.2 eV), presumably because it is harder to dope the inner tubes, which are protected by the outer walls. For the perpendicular case of as produced and ICl doped samples, a new peak appears around 0.8 eV, considered to be the inter subband plasmon peak [4].

Figure S8b schematically shows the E_F positions inferred from the results in Figure S8a. The calculated density of states (DOS) is shown for the outer and inner CNTs as a function of energy. See below for the calculation details. For the film annealed at 500 ˚C, E_F is expected to be in the vicinity of the first van Hove singularity (vHS) of the outer semiconducting tubes, as discussed above. The E_F of the film annealed at 350 ˚C is expected to be located at a slightly lower energy than the 500 ˚C case because an outer S_{11} peak is still observable, but the film annealed at 350 ˚C has higher σ than the film annealed at 500 ˚C. The E_F of the as-produced film is in the vicinity of the first vHS of the inner semiconducting CNTs, as S_{11} peaks of inner CNTs are still visible. The E_F of the film doped with ICl is expected to be at a slightly lower energy than the as-produced film, because an inner S_{11} peak is still observable but the ICl doped film has higher σ than the as-produced film.

Theoretical Calculations

From TEM analysis, the average outer wall diameter was 1.78±0.219 nm, and the average inner wall diameter was 0.92±0.12 nm. We chose four representative single-wall carbon nanotubes (SWCNTs) in Table S2 to describe double-wall carbon nanotubes (DWCNTs) used in this study.

We first calculated density of states DOS, conductance G, Seebeck coefficient S, and power factor $PF' \equiv GS^2$ for each SWCNT. Within the framework of the Landauer formula, the conductance $G(\mu)$ and Seebeck coefficient $S(\mu)$ with the chemical potential μ are expressed as

$$G(\mu) = \frac{2q^2}{h} \int dE\, T(E) \left(-\frac{\partial f(E,\mu)}{\partial E} \right) \tag{S1}$$

and

$$S(\mu) = \frac{1}{qT} \frac{\int dE\, T(E) \left(-\frac{\partial f(E,\mu)}{\partial E} \right) (E-\mu)}{\int dE\, T(E) \left(-\frac{\partial f(E,\mu)}{\partial E} \right)}, \tag{S2}$$

where q is the charge of carriers, h is the Planck constant, $f(E, \mu)$ is the Fermi–Dirac distribution function, and $T(E)$ is the transmission function. As can be seen here, we can obtain $G(\mu)$ and $S(\mu)$, once $T(E)$ is calculated.

We used the tight-binding method to calculate the thermoelectric properties of isolated SWCNTs in Table S2 with 1×1×9 Monkhorst-Pack K-grid. The Slater–Koster parameters used in this method were obtained by the density-functional tight-binding method utilizing the "hotbit" code [5]. Using these parameters, we performed the calculation of density of states (DOS) for bulk SWCNTs. In addition, $T(E)$ of SWCNTs was calculated by combing the nonequilibrium Green's function method with the tight-binding method. SWCNTs were divided into three regions; device region, a left electrode, and a right electrode. The length of the device region is five unit cells for (11,0), (22,0), (6,6), and (13,13) SWCNT. The above-mentioned calculation was implemented in the ATK-SE package (Ver. 2017.2) [6]. Calculated DOS, G, S, and PF' for each SWCNT are shown in Figure S9.

As discussed in previous studies [7,8], peaks of S of semiconducting SWCNTs appear inside the bandgap near the charge neutrality point (CNP), where chemical potential is 0 eV (Figure S9a and B), while that of metallic SWCNTs appear near the first van Hove singularity (vHS) (Figure S9d). On the other hand, the peaks of PF' of both semiconducting and metallic SWCNTs are located near the vHS. Note that M1 does not show a peak in Figure S9c solely due to limited chemical potential range. Although there is a nearly one order difference in S values between semiconducting and metallic SWCNTs, the maximum values of PF' are on the same order, which is consistent with Ref [7].

Next, we use simple circuit models suggested in [8–10] to approximate our DWCNT fiber. As shown in Figure S10, one SWCNT is considered to be a combination of a generator ($S_i \Delta T$) and a resistor ($R_i = 1/G_i$), where i denotes that this is the ith nanotube in the system. For simplicity, we assume that temperature difference applied per one nanotube ΔT and Δt are the same for all nanotubes. The ratio of semiconducting to metallic was assumed to be 2:1 since we did not conduct any chirality enrichment. By using the parallel circuit model shown in Figure S10b, the total Seebeck coefficient and conductance of the entire system can be written as [8–10]:

$$S = \frac{\sum_i S_i G_i}{\sum_i G_i} \quad \text{and} \quad G = \sum_i G_i \tag{S3}$$

Thus, based on the ratio of semiconducting to metallic nanotubes (2:1), Seebeck coefficient S_p and conductance G_p of our system can be expressed as

$$S_p = \frac{2S_{\mathrm{S1}}G_{\mathrm{S1}} + 2S_{\mathrm{S2}}G_{\mathrm{S2}} + S_{\mathrm{M1}}G_{\mathrm{M1}} + S_{\mathrm{M2}}G_{\mathrm{M2}}}{2G_{\mathrm{S1}} + 2G_{\mathrm{S2}} + G_{\mathrm{M1}} + G_{\mathrm{M2}}}, \tag{S4}$$

and

$$G_p = \frac{2}{6}G_{\mathrm{S1}} + \frac{2}{6}G_{\mathrm{S2}} + \frac{1}{6}G_{\mathrm{M1}} + \frac{1}{6}G_{\mathrm{M2}}, \tag{S5}$$

where S_{S1} is Seebeck coefficient of S1 nanotube, G_{S1} is the electrical conductance of S1 nanotube, and similarly for S2, M1, and M2 nanotubes.

For a series circuit model case as shown in Figure S10c, the total Seebeck coefficient and conductance of the entire system can be written as [8–10]

$$S = \sum_i S_i \quad \text{and} \quad \frac{1}{G} = \sum_i \frac{1}{G_i}. \tag{S6}$$

For the series case, with a 2:1 ratio of semiconducting to metallic CNTs, the Seebeck coefficient S_s and conductance G_s of our system can be expressed as

$$S_s = \frac{2}{6}S_{\mathrm{S1}} + \frac{2}{6}S_{\mathrm{S2}} + \frac{1}{6}S_{\mathrm{M1}} + \frac{1}{6}S_{\mathrm{M1}}, \tag{S7}$$

and

$$G_s = \left(\frac{2/6}{G_{\mathrm{S1}}} + \frac{2/6}{G_{\mathrm{S2}}} + \frac{1/6}{G_{\mathrm{M1}}} + \frac{1/6}{G_{\mathrm{M2}}}\right)^{-1}. \tag{S8}$$

Figure S11 shows states G, S, PF', and DOS calculated for a parallel circuit case using Equation (S4) and (S5). The chemical potential range examined was determined based on the optical study discussed in Figure S8. G has finite values even inside the bandgap, as shown in Figure S11a, because the total conductance of the system is simply the sum of the conductance from each contribution in the parallel case (Equation (S5)). S is drastically reduced especially inside the bandgap of S1 and S2 (Figure S11b and e) because Equation (S4) can be approximated as

$$S \approx \frac{S_{\mathrm{M1}}G_{\mathrm{M1}} + S_{\mathrm{M2}}G_{\mathrm{M2}}}{G_{\mathrm{M1}} + G_{\mathrm{M2}}} \tag{S9}$$

within the bandgap due to $G_{S1} \approx G_{S2} \approx 0$. Thus, instead of having peaks near the charge neutral point, peaks appear near vHS of S1 and S2 as discussed in Ref [8]. PF' has peaks in the vicinity of vHS as shown in Figure S11c but smaller in amplitude compared to individual cases, again consistent with Ref [8]. The smaller amplitude is due to having metallic tubes and having two different diameter distributions. When sweeping chemical potential from 0 eV into bands (either negative or positive), the Figure S11c shows that the first peak around ±0.2 eV is given by S2 and the second peak around ±0.4 eV is given by semiconducting tubes (S1 and S2). Figure S11f and G shows S and PF' as a function of G respectively, showing multiple peaks in both shows S and PF' (mainly two peaks within the region examined) with increasing G.

Figure S12 shows G, S, PF', and DOS calculated for a series circuit case using Equation (S7) and (S8). Conductance G is greatly reduced in the bandgap range of S2, because G_s can be approximated as

$$G_s = \left(\frac{2}{G_{\mathrm{S1}}} + \frac{2}{G_{\mathrm{S2}}} + \frac{1}{G_{\mathrm{M1}}} + \frac{1}{G_{\mathrm{M2}}}\right)^{-1} \approx 0 \tag{S10}$$

when $G_{S1} \approx G_{S2} \approx 0$ (Figure S12a). Unlike parallel case, the maximum value of S is located near CNP, and its amplitude is comparable to S2 case (Figure S12b) because S is simply the sum of the Seebeck coefficient from each contribution in series case (Equation (S7)). PF' is almost zero in the bandgap of S2 because G_s is largely suppressed in the range, and its amplitude is similar to the parallel case (Figure S12c). Figure S12f and g shows S and PF' as a function of G respectively, showing a single peak within the region examined with increasing G, drastically different from the parallel case where there were multiple peaks (Figure S11f and g).

The series case does not reproduce our experimental results well. Figures 1c and d demonstrates that both Seebeck coefficient S and power factor PF decreases with increasing conductivity σ, but Figure S12g shows ${PF'}_s$ increases with the increase of the conductance G_s. Furthermore, our gating measurement (Figure S3) suggests that there is more than one peak in S and PF as a function of σ, contradicting to Figure S12f and g.

The parallel case reproduces our data better, as pointed out in Ref. [8,11], but it has some discrepancies too. First, ${PF'}_p$ as a function of G_p shows that the second peak is higher than the first peak (Figure S11g), but Figure 1d suggests that PF monotonically decreases with σ. Second, as shown in Figure 2f, S value sharply increase right after the charge neutrality point, which Figure S11a, b and c fail to reproduce.

Thus, we considered combining the parallel model and the series model, which is reasonable because there are both parallel and series connections existing inside our fiber. We used the model suggested in Ref [12] for combining the Seebeck coefficient,

$$S_{\mathrm{tot}} = (1-\beta)S_{\mathrm{s}} + \beta S_{\mathrm{p}}, \tag{S11}$$

where S_{tot} is the combined Seebeck coefficient, S_{s} is the Seebeck coefficient from the series model, S_{p} is the Seebeck coefficient from the parallel model, and β is the fraction of parallel component, which will be optimized to describe our system the best. This equation of combining the series and parallel model is analogy to the Equation (S6), where nanotubes were connected in the series way. Thus, we used the series model to combine conductance as the following:

$$G_{\mathrm{tot}} = \left(\frac{1-\alpha}{G_{\mathrm{s}}} + \frac{\alpha}{G_{\mathrm{p}}}\right)^{-1} \tag{S12}$$

where G_{tot} is the combined conductance, G_{s} is the conductance from the series model, G_{p} is the conductance from the parallel model, and α is the fraction of parallel component, which will be optimized to describe our system the best.

We first tuned α while fixing $\beta = 1$. Figure S13a and c show G and PF' with an α of 0 to 0.9 varied by 0.1 increments.. As shown in Figure S13a, G_{s} is dominant even at $\alpha = 0.9$, resulting in PF' behavior analogy to series model, having near zero PF' inside S2 bandgap. This scenario applies even for the $\alpha = 0.99$ case as shown in Figure S13e and g. However, a small peak from PF' starts to appear around the first vHS of S2. Moreover, according to our experimental data, the

peak of PF' around the first S2 vHS has to be larger or comparable to the peak around the first S1 vHS. Therefore, we decided to fix α at 1. We also tuned α while fixing $\beta = 0$, again there was no peak of PF' around the first S2 unless $\alpha \approx 1$ (data not shown).

Next, we tuned β while fixing $\alpha = 1$. Figure S14b and c shows S and PF' with a β of 0 to 1 varied by 0.1 increments. As shown in Figure S14b, the first peak of S around the CNP (marked by *) is suppressed with increasing β, while the second peak around the first vHS of S2 (marked by †) becomes more dominant. PF' also shows two peaks (* and †) between CNP and vHS of S2 (Figure S14c). The first peak (*) arises, which was absent in series case, arises because of finite G even withing the bandgap. It gets suppressed with increasing β, while the second peak (†) becomes more dominant.

Figure S15 shows S and PF' as a function of G with changing β. The first peak (*) looks sharp because G is nearly a constant inside the S1 bandgap (Figure S14a). A dip around G of around 1×10^{-4} S is not apparent for small β for both S and PF'.

We chose $\beta = 0.9$ for our model. First, $\beta = 0 - 0.9$ cases satisfy two points which the parallel model failed to reproduce; PF' shows overall decrease with G in (Figure S15b), and both S and PF value sharply increase right after the CNP as shown in Figure S14f and g. However, the first peak (*) is too dominant with $\beta = 0 - 0.8$ in Figure S15 when compared with our gating data (Figure S3). Thus, we used $\alpha = 1$ and $\beta = 0.9$ to approximate our DWCNT fiber.

In order to verify our method, we used our model to reproduce results from Ref. [7]. In this study, the authors used two types of SWCNTs, (6,5) semiconducting SWCNT with diameter of 0.76 nm and metallic enriched SWCNTs with the average diameter of 1.40 nm. Their sample 1 (#1) was >99% (6,5), sample 2 (#2) was mixture of 90% (6,5) and 10% metal, sample 3 (#3) was 50% (6,5) and 50% metal, sample 4 (#4) was >99% metal, and sample 5 (#5) was aligned metal. S shows its maximum value around gate voltage of 0 V only for #1, and other samples show maximum S value at higher (#2) or at the highest (#3-5) gate voltage. As shown in Figure 2b of Ref. [7], S shows a sharp value change around gate voltage of 0 V for #1, and #2-#5 also show a finite change although the amplitude is not as large as #1. PF is nearly zero at small gate voltage, and shows a peak (#1 and #2) or increases with gate voltage (#3-5) (Figure 2c of Ref. [7]).

In our model, we used S1 in Table S2 as (6,5) SWCNT and M2 as metallic SWCNTs. We set the ratio of S1 to M2 as 100:0 for #1, 10:90 for #2, 50:50 for #3, and 0:100 for #4. We set $\alpha = 1$ and $\beta = 0.99$ for #2 and #3.

Figure S16a and b show S and PF', respectively as a function of chemical potential for sample #1 to #4. Overall, our model adequately reproduces Figure 2 of Ref. [7] qualitatively. S shows its maximum value around CNP only for #1, and other samples show peaks around the first vHS. In Figure 2b of Ref. [7], S monotonically increased with gate voltage for #3 and 4 because the gated range was not wide enough to obtain the peaks. Note that the tuned chemical potential range differs from sample to sample even when the same gate voltage range was used. PF is nearly zero at and show its peak around first vHS (Figure S16). Remarkably, our model was able to reproduce a small jump-like behavior around the charge neutrality point for #2 and 3, by including a small percentage

(1%) of the series model. As shown in Figure S17, it fails to reproduce this behavior without including the series model ($\beta = 1$).

Device Characterizations

From fitting the voltage versus temperature curve of Figure 3d, the slope is 0.00132 V/K. Since there were 60 CNT threads in the device, the Seebeck coefficient of each CNT thread is estimated to be 22.1 μV/K. This value is lower than the highest value in Figure 1c (>60 μV/K) because there was no prior chemical treatment to optimize the Fermi energy position.

Figure S6a shows measured voltage drops across the loaded resistors V_{L} (calculated power P_{L}) as a function of measured current I_{tot} on the left (right) axis at each temperature. V_{L}, I_{tot} and P_{L} can be described as

$$I_{\mathrm{tot}} = \frac{V_{\mathrm{tot}}}{R_{\mathrm{CNT}} + R_{\mathrm{L}}} \tag{S13}$$

$$V_{\mathrm{L}} = R_{\mathrm{L}} \times \frac{V_{\mathrm{tot}}}{R_{\mathrm{CNT}} + R_{\mathrm{L}}}, \tag{S14}$$

$$P_{\mathrm{L}} = V_{\mathrm{L}} \times I_{\mathrm{tot}} \tag{S15}$$

where V_{tot} is the total voltage generated by the thermoelectric generator, R_{CNT} is the resistance of the thermoelectric generator, and R_{L} is the resistance of the loaded resistor. V_{tot} is defined as $V_{\mathrm{tot}} = S \times \Delta T \times N$, where S is the Seebeck coefficient of each CNT thread (=22.1 μV/K in this case as described above), ΔT is the temperature difference applied, and N is the number of CNT threads ($N = 60$). We fit V_{L} versus I_{tot} using Equations S13 and S14 with R_{CNT} as a fitting parameter. We allowed R_{CNT} to change with the temperature. As shown in Figure S6a, the fitting and the measured values show excellent agreement. Figure S6b shows P_{L} as a function of R_{L} at ΔT of 62.5 K to show that P_{L} is maximized when $R_{\mathrm{L}} = R_{\mathrm{CNT}}$.

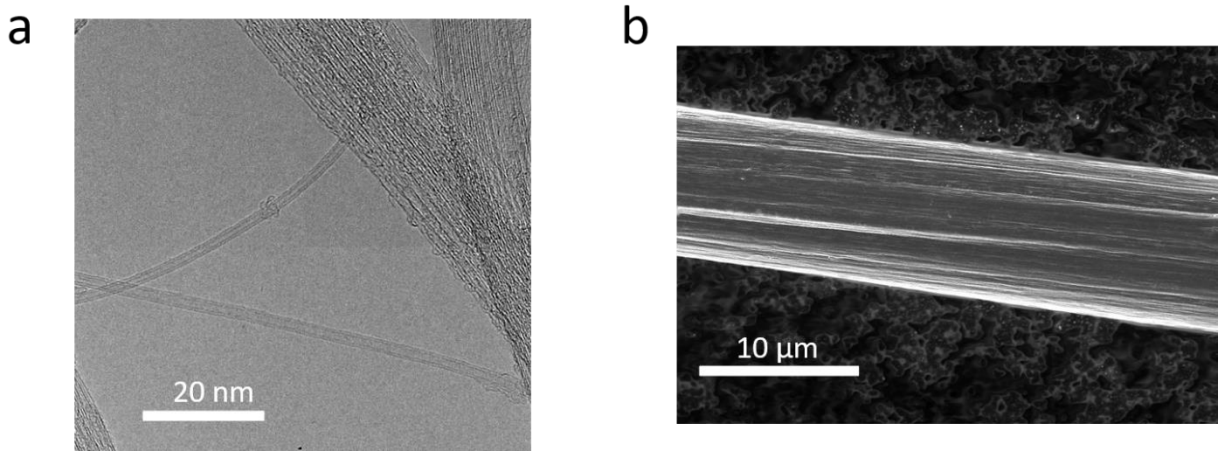

Figure S1. (a) HR-TEM image of the raw CNT material. (b) SEM image of the surface morphology of the fiber produced by solution spinning method, depicting highly aligned CNT bundles.

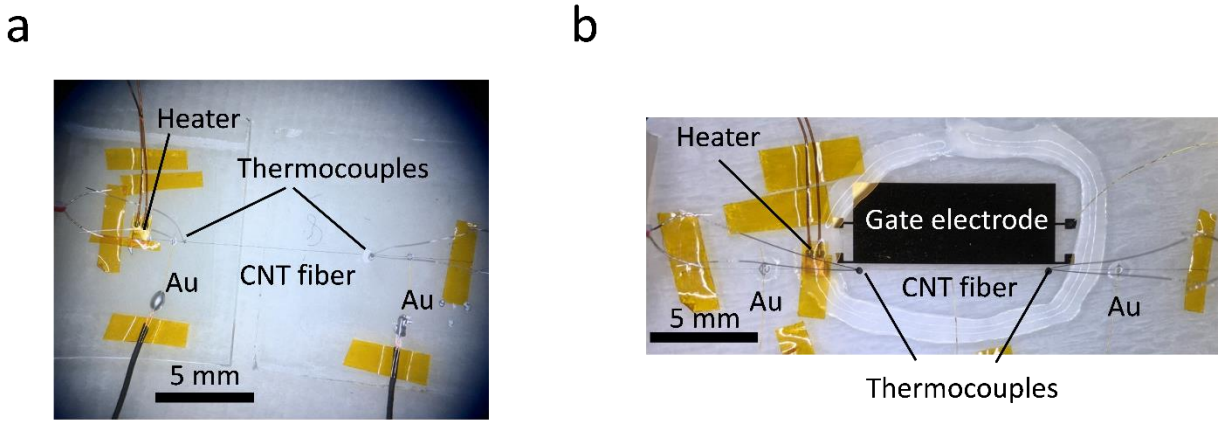

Figure S2. (a) Picture of a device used on a chemically treated sample without gating. (b) Picture of a device used for the gating measurement.

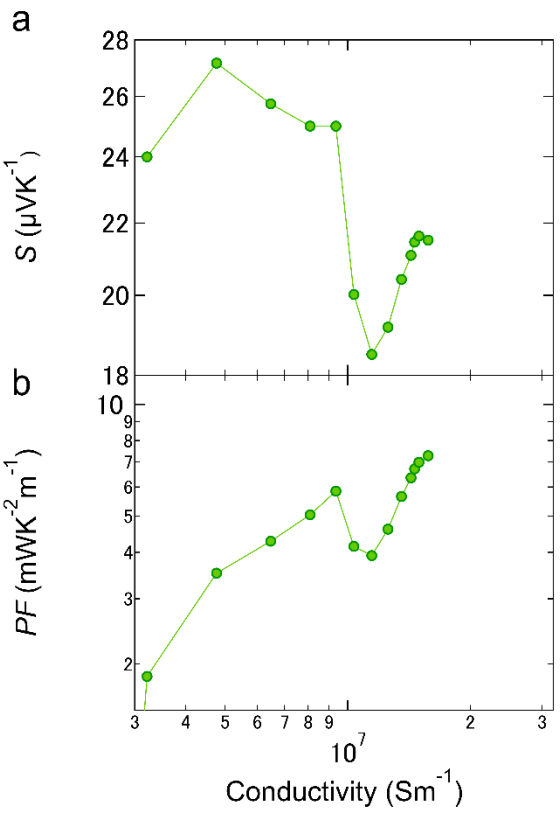

Figure S3. (a) S and (b) PF of p-side from a gating experiment as a function of measured electrical conductivity.

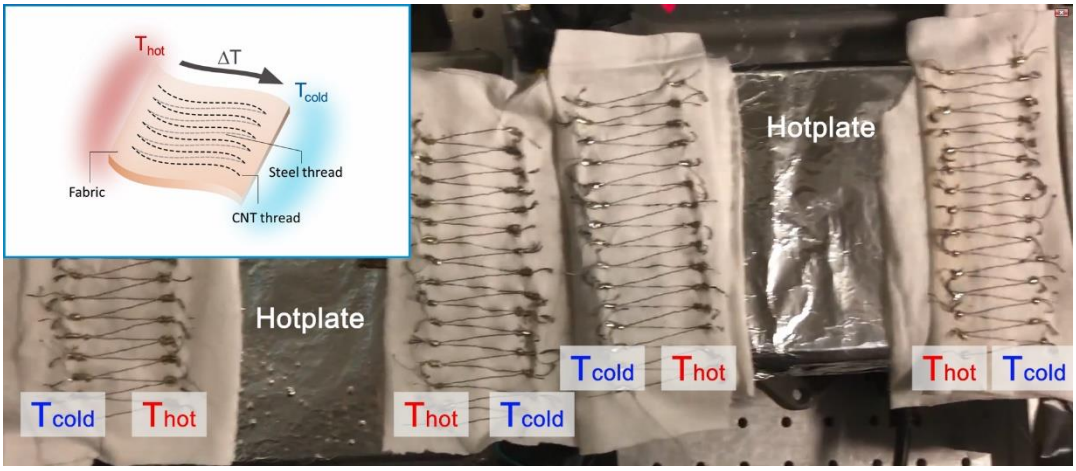

Figure S4. The CNT thread and steel thread were sewn into a fabric. Fifteen CNT threads were connected thermally in parallel and electrically in series to create one TEG unit, and the four units were connected in series. The cold side was at room temperature, and the hot side was placed on hotplates. The inset shows the schematic image of a textile TEG.

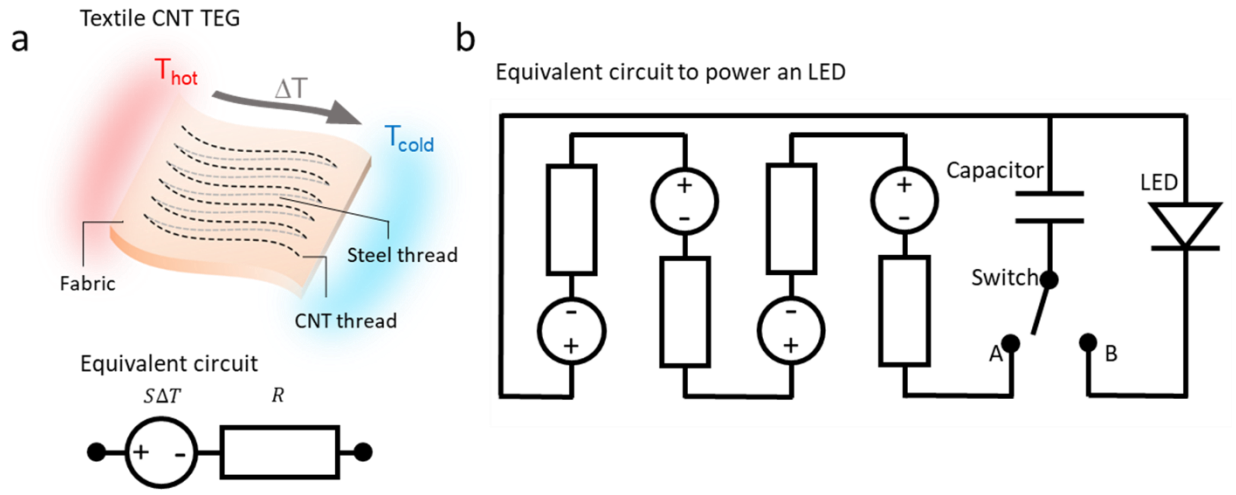

Figure S5. (a) One TEG unit is equivalent to a voltage source and a resistor. (b) The entire circuit to power the LED consists of four TEG units connected in series, a capacitor, an LED, and a switch. When the switch is connected to A, the capacitor is charged by the TEGs. When it switches to B, the capacitor discharges and lights up the LED.

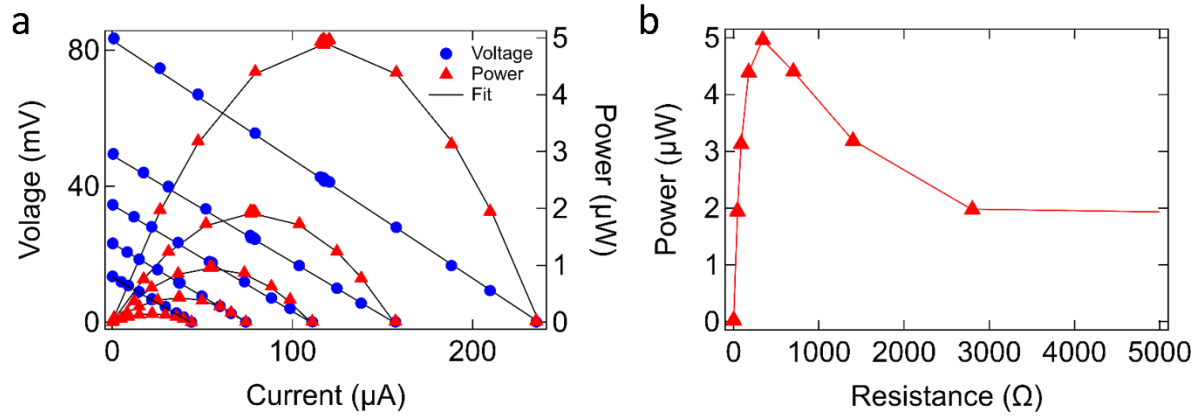

Figure S6. (a) The output voltage and power at temperature differences, fitted by Equation S13-15. (b) The output power as a function of loaded resistance at a temperature difference of 62.5 K.

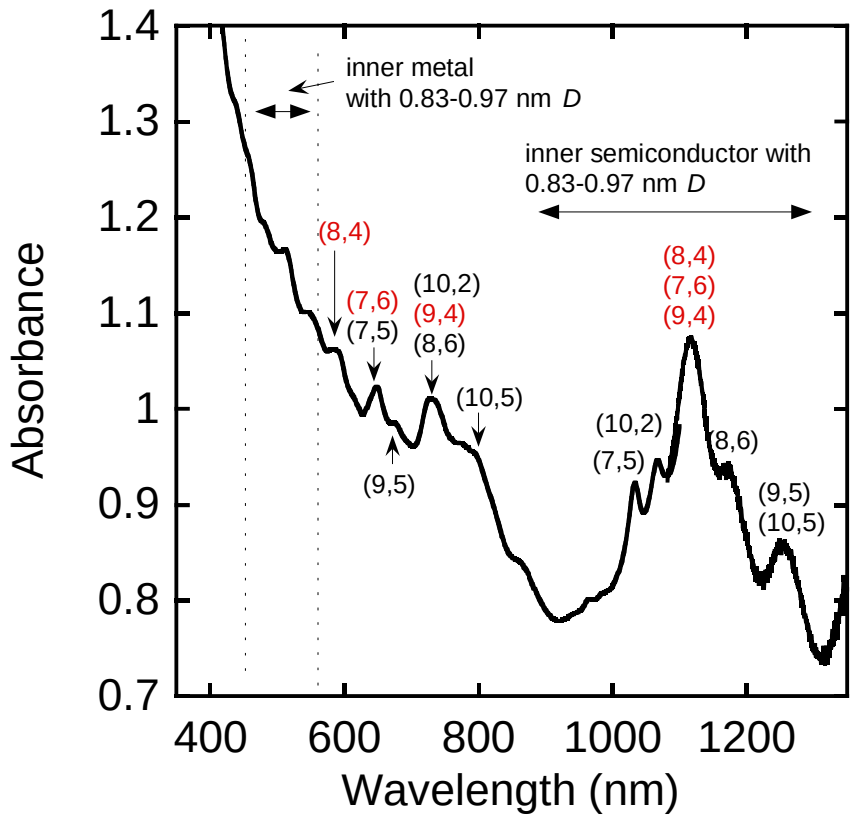

Figure S7. Absorbance spectrum of the solution of the raw CNT material. Chirality of inner wall nanotubes were assigned based on Ref [2,3].

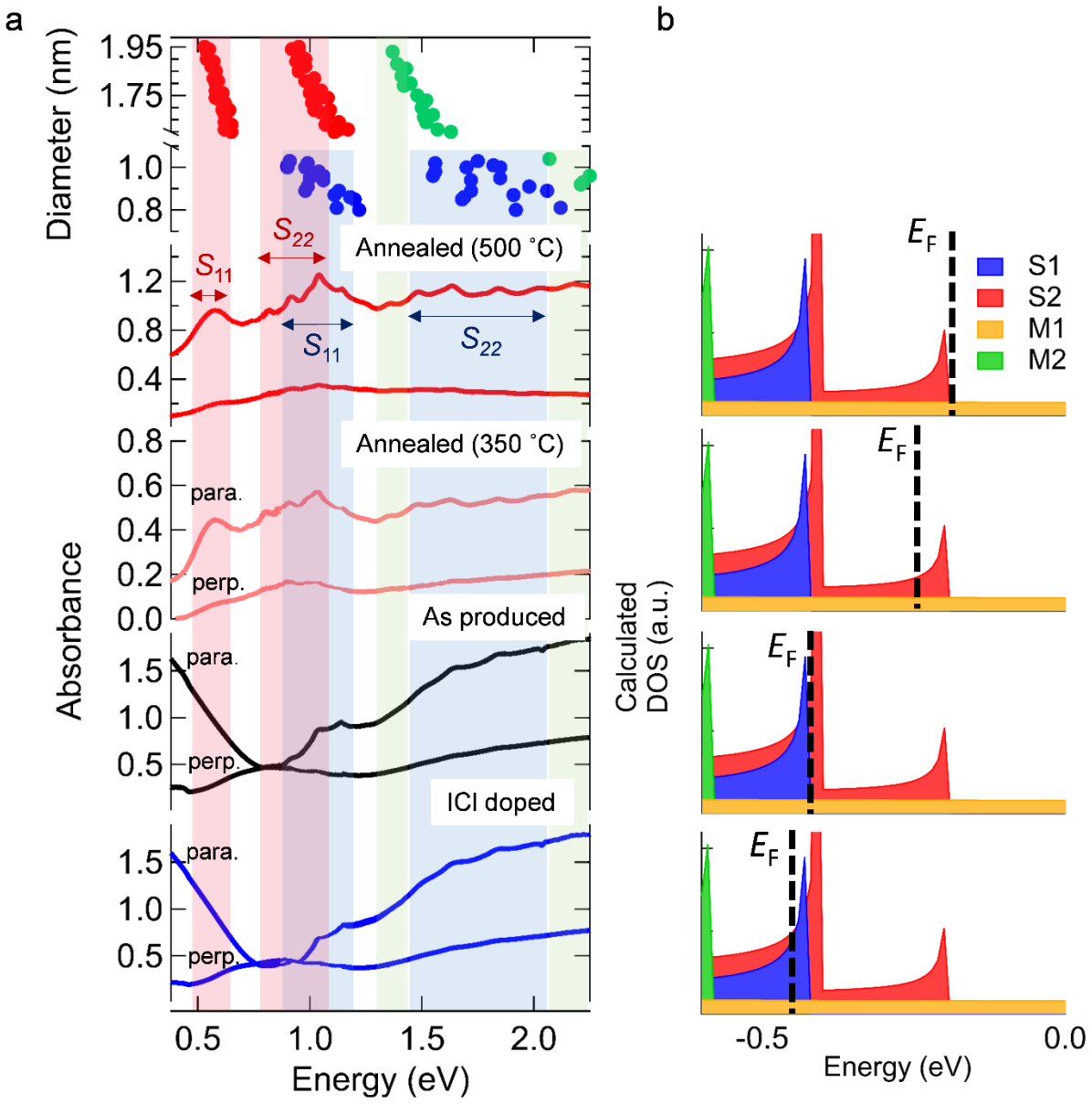

Figure S8. Optical studies of CNTs aligned films. (a) (Top) Expected absorbance peak positions based on diameter information from Ref [2,3], including transition peaks due to the outer semiconducting tubes (marked as S_{11} and S_{22}, red), inner semiconducting tubes (blue), and outer and inner metallic tubes (M_{11}, green). (Bottom) Absorbance spectra of CNT films with the same chemical treatments as Figures 1c and d; annealing at 500 ˚C, annealing at 350 ˚C, as produced, and ICl doping. For each sample, both parallel (when the incident light polarization was parallel to the CNT alignment direction) and perpendicular (when the incident light polarization was perpendicular to the CNT alignment direction) are shown. For the perpendicular case of as produced and ICl doped samples, a new peak appears around 0.8 eV, considered to be the inter subband plasmon peak [4]. (b) Calculated density of states (DOS) as a function of energy, for S1, S2, M1, and M2 (see Table S2 for their definition.) The expected E_F position deduced from analysis of the spectra in (a) is shown by the black dashed line in each case.

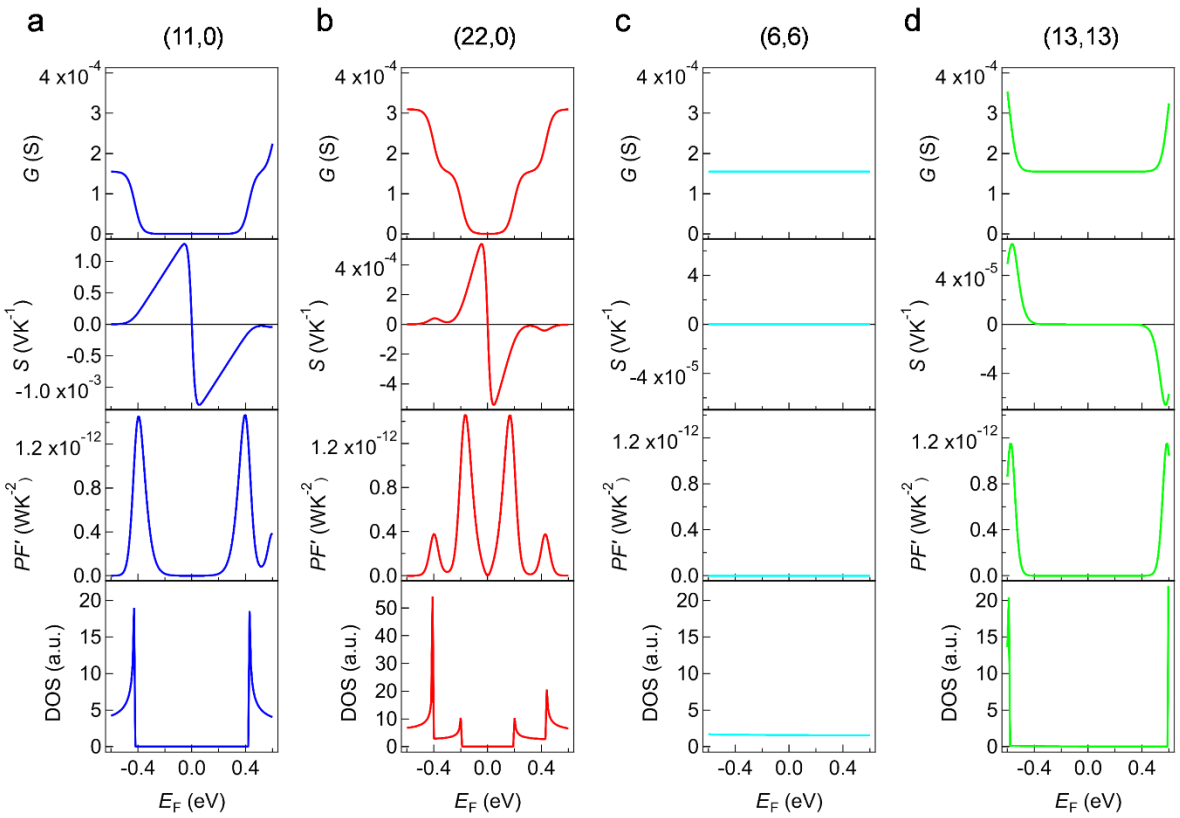

Figure S9. Calculated G, S, and PF' for four representative SWCNTs, (a) S1 (11,0), (b) S2 (22,0), (c) M1 (6,6) and (d) M2 (13,13).

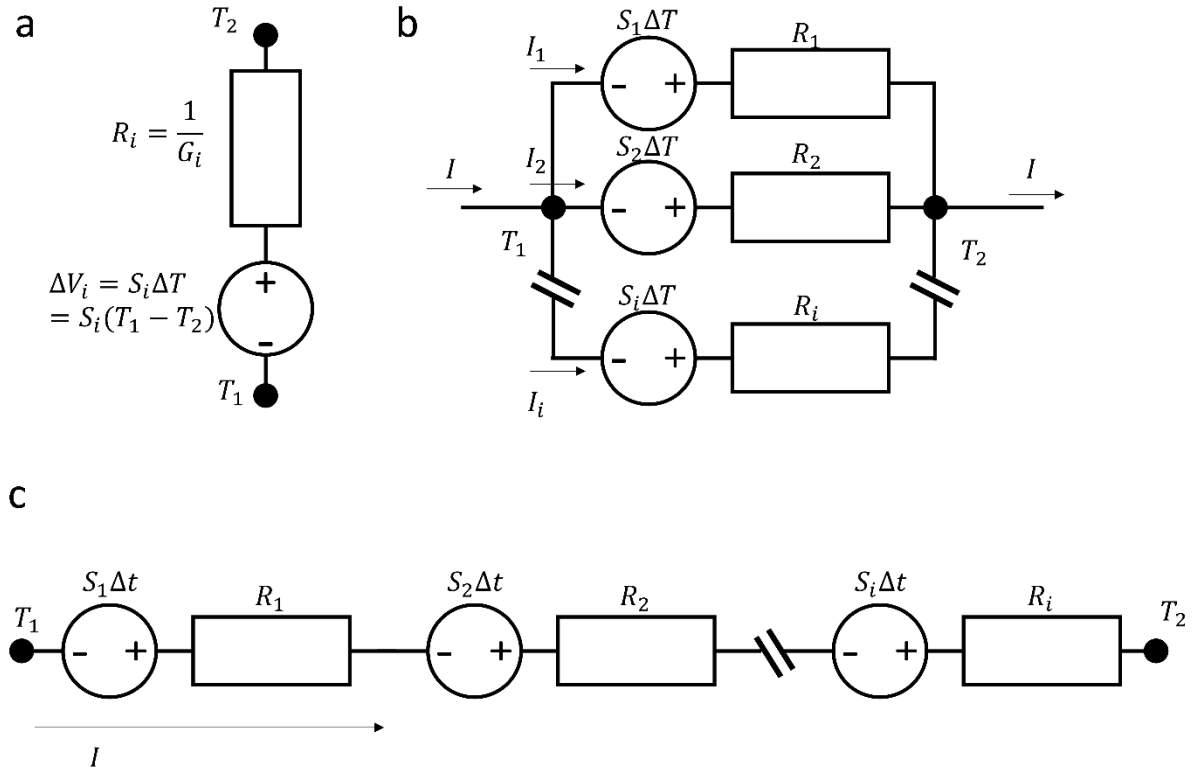

Figure S10. Circuit models used to approximate the DWCNT system. (a) Each SWCNT is approximated by an equivalent circuit components of a generator ($S_i\Delta T$) and a resistor ($R_i = 1/G_i$), where i denotes that this is the ith nanotube in the system. (b) Nanotubes described in (a) are connected in parallel. A temperature gradient applied per one nanotube ΔT is assumed to be the same for all nanotubes for simplicity. (c) Nanotubes described in (a) are connected in series. A temperature gradient applied per one nanotube Δt is assumed to be the same for all nanotubes.

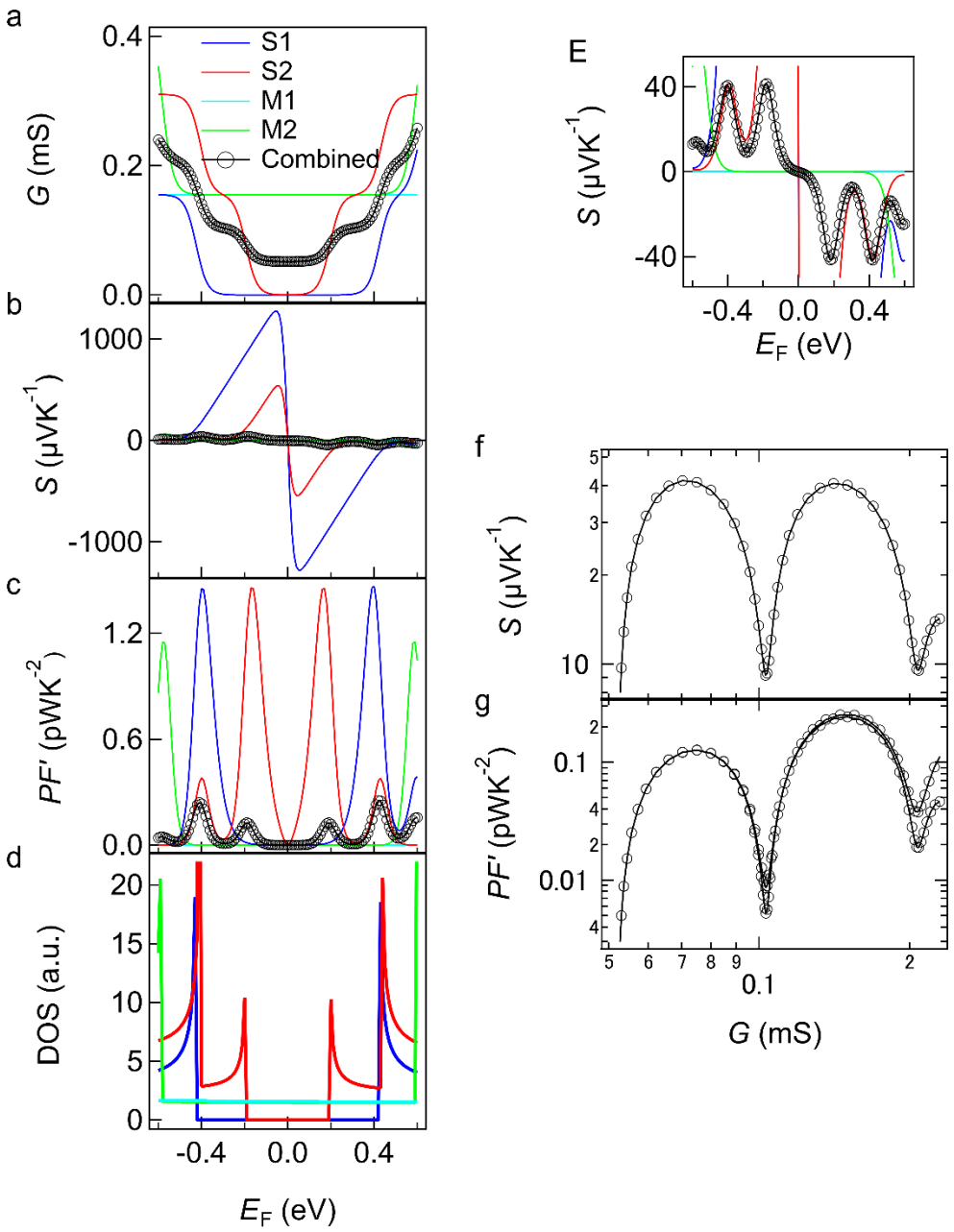

Figure S11. Calculated results using a parallel circuit model using Equation (S4) and (S5). Calculated (a) G, (b) S, and (c) PF' combining four SWCNTs using a parallel model as a function of chemical potential shown in a black line with open circles. G, S, and PF' of S1 (blue), S2 (red), M1 (cyan), and M2 (green) from Figure S9 are shown for a comparison. (d) Density of states of S1 (blue), S2 (red), M1 (cyan), and M2 (green). (e) Magnified image of Figure S11b. (f) S and (g) PF' of combined result as a function of G.

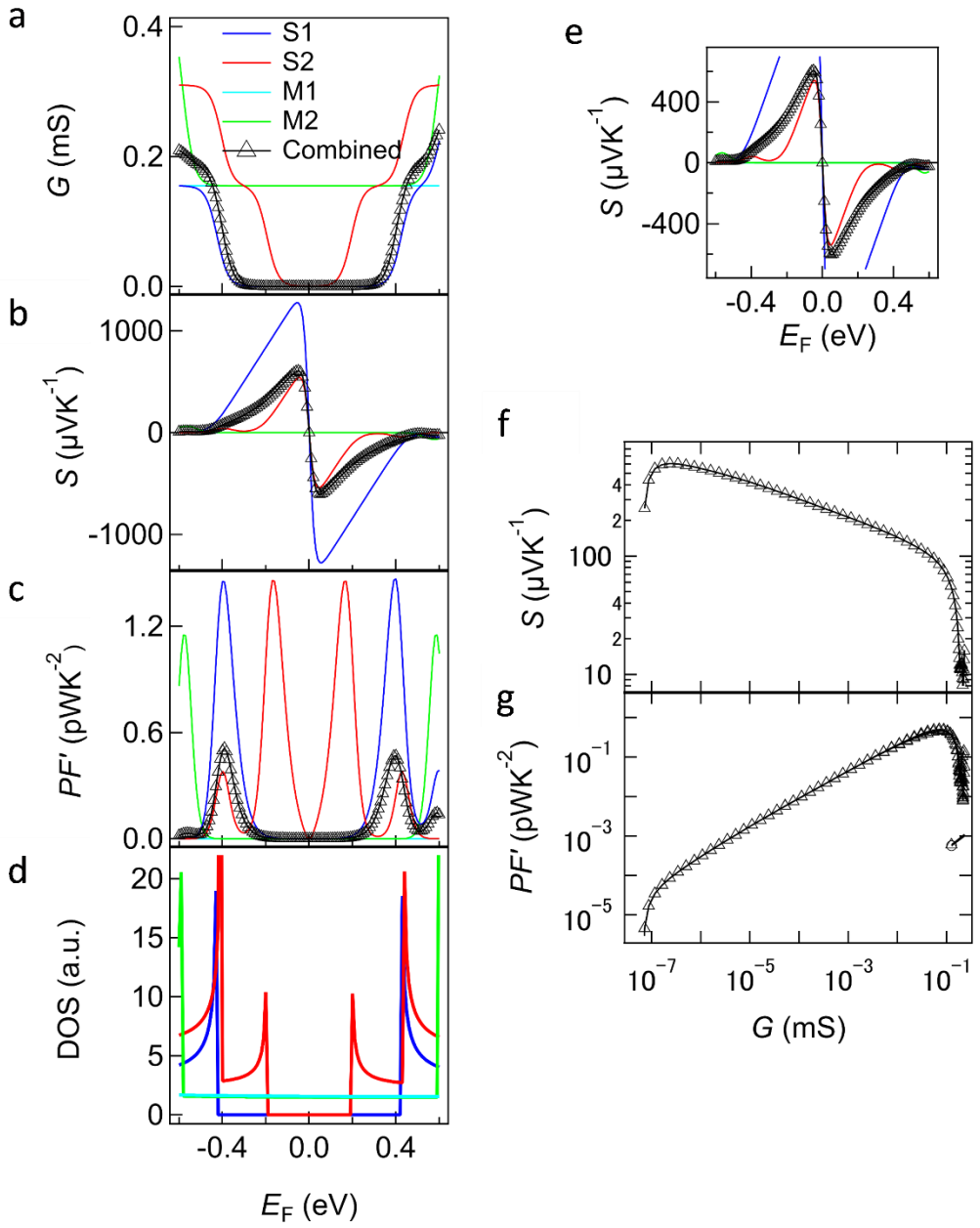

Figure S12. Calculated results using a series circuit model using Equation (S7) and (S8). Calculated (a) G, (b) S, and (c) PF' combining four SWCNTs using a series model as a function of chemical potential shown in a black line with open circles. G, S, and PF' of S1 (blue), S2 (red), M1 (cyan), and M2 (green) from Figure S9 are shown for a comparison. (d) Density of states of S1 (blue), S2 (red), M1 (cyan), and M2 (green). (e) Magnified image of Figure S12b. (f) S and (g) PF' of combined result as a function of G.

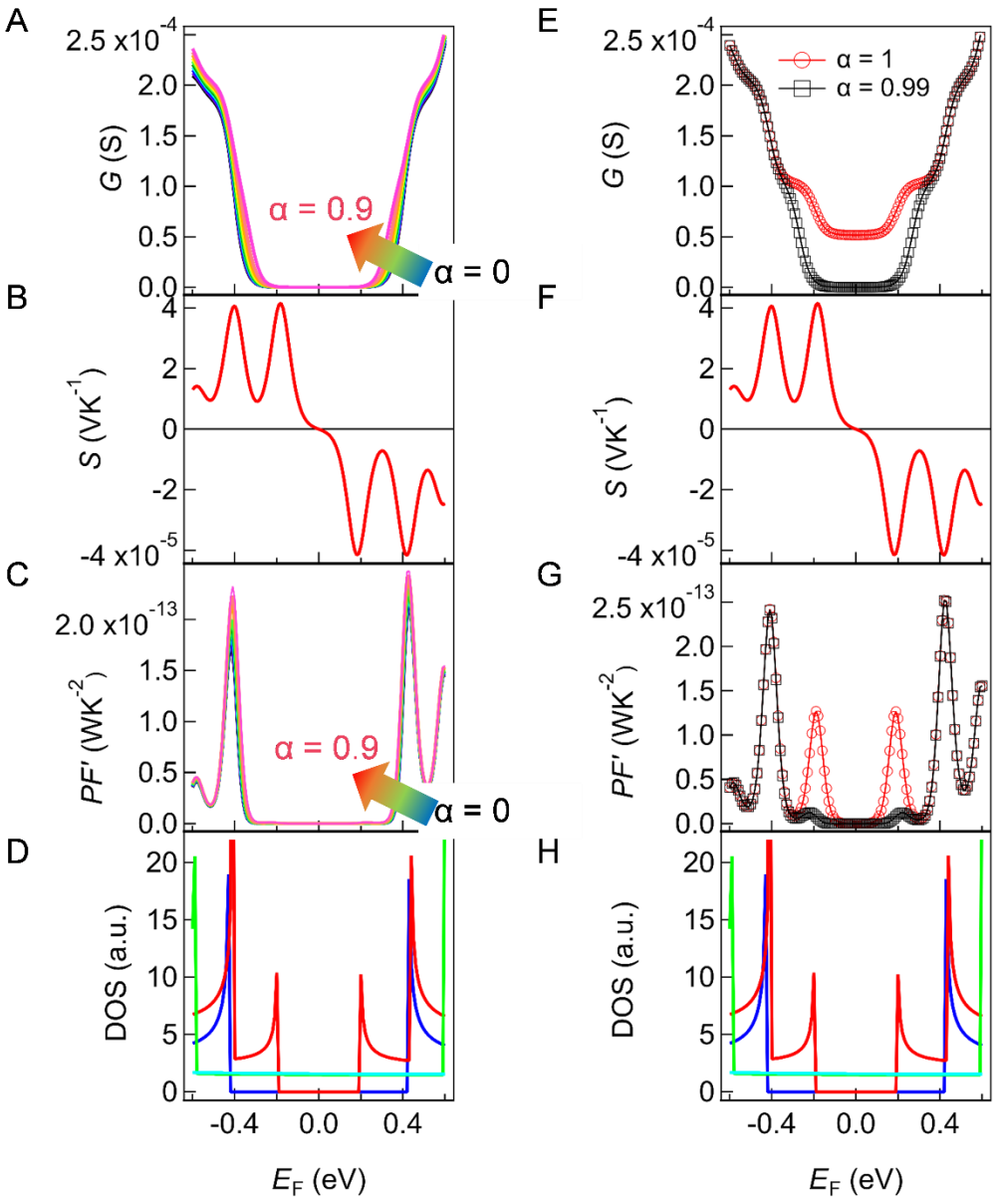

Figure S13. Tuning α in Equation (S12). Calculated (a) G, (b) S, and (c) PF' as a function of chemical potential with α of 0 to 0.9 by 0.1 while fixing $\beta = 1$. (d) Density of states of S1 (blue), S2 (red), M1 (cyan), and M2 (green). Calculated (e) G, (f) S, and (g) PF' as a function of chemical potential with α of 0.99 and 1 while fixing $\beta = 1$. (h) Density of states as a reference.

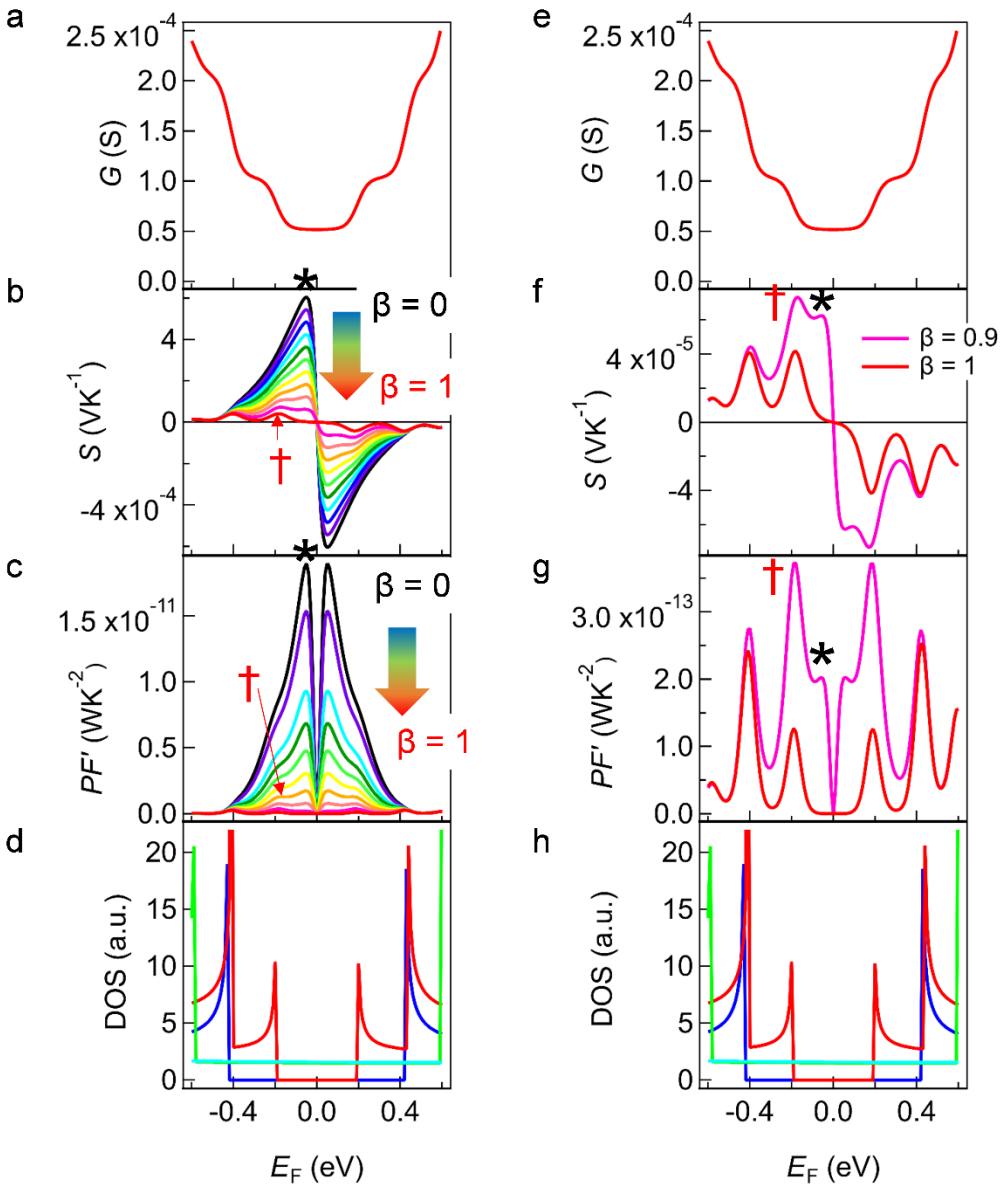

Figure S14. Tuning β in Equation (S11). Calculated (a) G, (b) S, and (c) PF' as a function of chemical potential with β of 0 to 1 by 0.1 while fixing $\alpha = 1$. (d) Density of states of S1 (blue), S2 (red), M1 (cyan), and M2 (green). Calculated (e) G, (f) S, and (g) PF' as a function of chemical potential with β of 0.9 and 1 while fixing $\alpha = 1$. (h) Density of states as a reference.

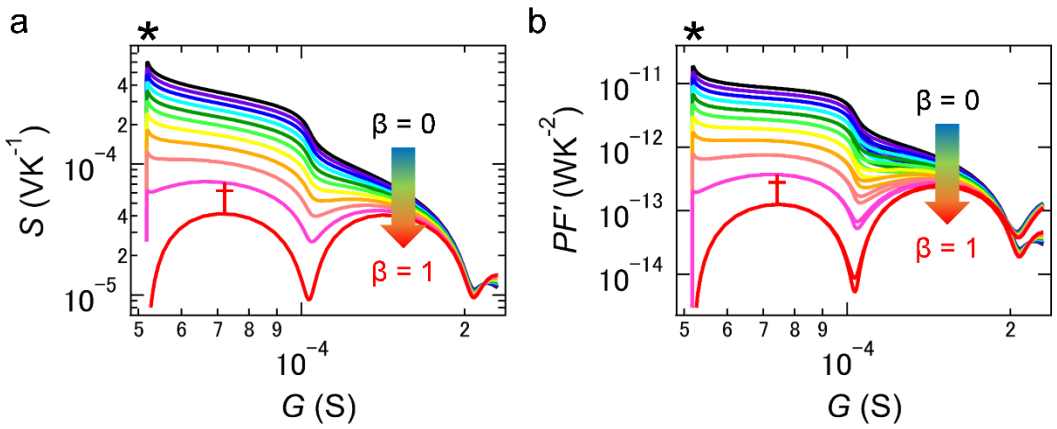

Figure S15. (a) S and (b) PF' as a function of G with β of 0 to 1 by 0.1 increments while fixing $\alpha = 1$ from Equation (S11).

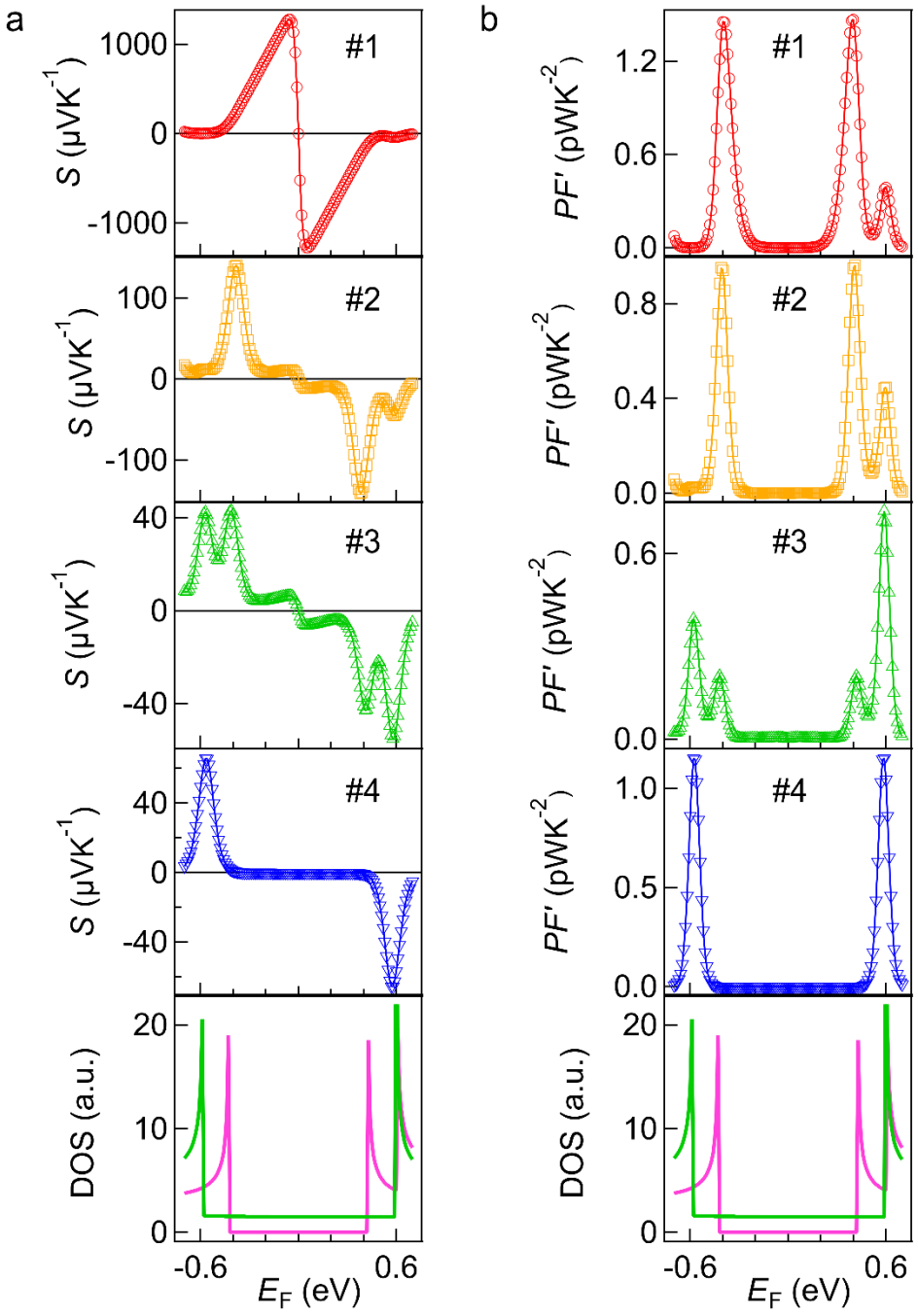

Figure S16. Calculated (a) S, and (b) PF' as a function of chemical potential. #1 is the same as S2 in Figure S9 and #4 is the same as M1 in Figure S9. For #2 and #3, we used the parallel and series combined model with $\beta = 0.99$ (Equation (S11)) and $\alpha = 1$ from Equation (S12). The ratio of S2:M1 is 90:10 for #2 and 50:50 for #3. DOS of S2 and M1 is shown as a reference.

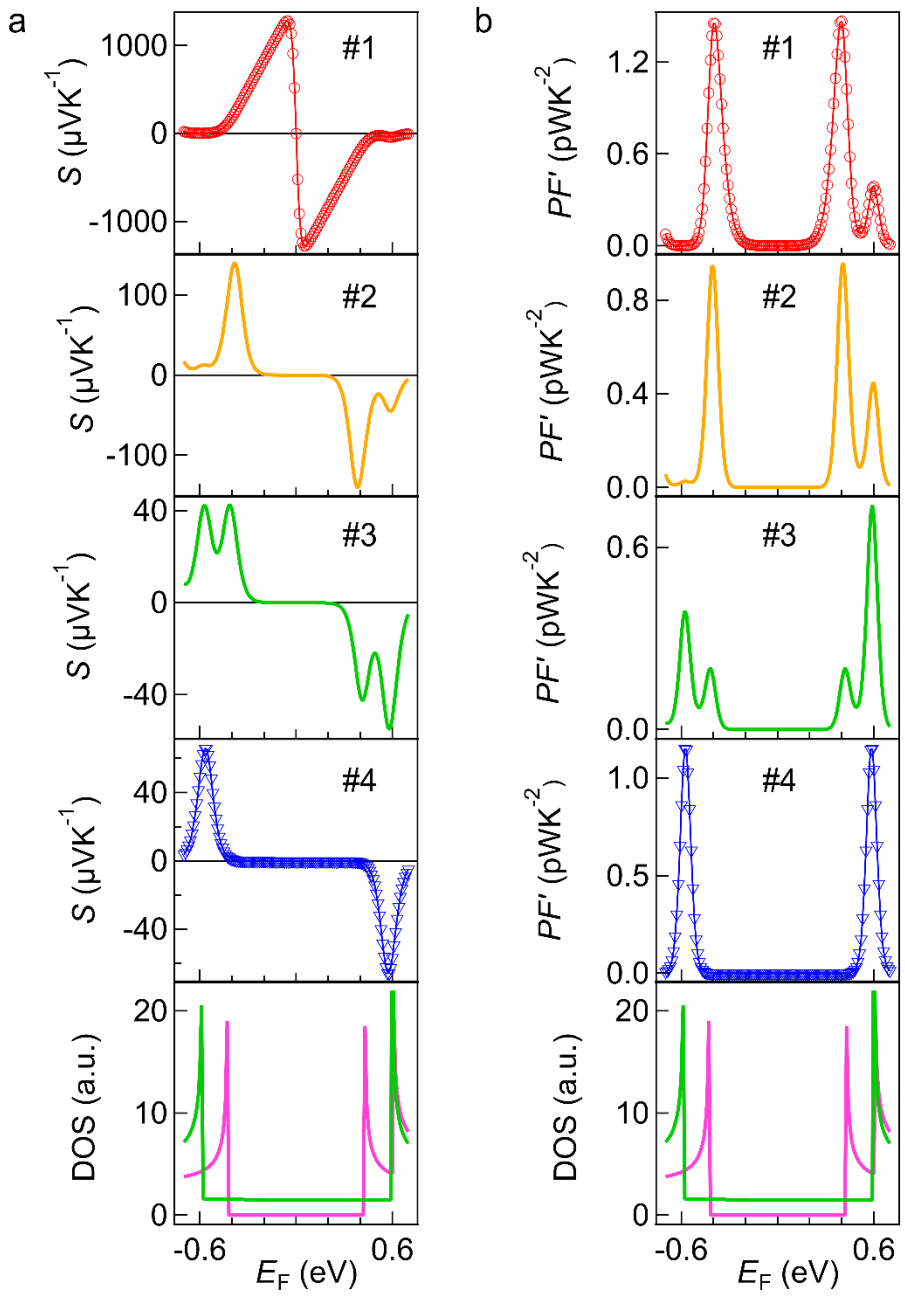

Figure S17. Calculated (a) S, and (b) PF' as a function of chemical potential. #1 is the same as S2 in Figure S9 and #4 is the same as M1 in Figure S9. For #2 and #3, we used the parallel and series combined model with $\beta = 1$ (Equation (S11)) and $\alpha = 1$ from Equation (S12). The ratio of S2:M1 is 90:10 for #2 and 50:50 for #3. DOS of S2 and M1 is shown as a reference.

Table S1. Four types of samples measured with different chemical treatments

Chemical treatment	Electrical conductivity (MS/m)	Seebeck coefficient (μV/K)	Power factor ($\mu W/mK^2$)
ICl doped	15.6±3.04	18.0±0.226	5,070±987
N/A (as produced)	11.3±2.19	21.5±0.183	5,210±1,010
Annealed at 350 ˚C	5.55±1.08	31.7±0.175	5,580±1,080
Annealed at 500 ˚C	2.69±0.522	68.0±0.293	12,400±2,420

Table S2. Four representative SWCNTs used to describe DWCNT fiber

	Chirality	Diameter (nm)	Electronic type
S1	(11,0)	0.87	Semiconducting
S2	(22,0)	1.75	Semiconducting
M1	(6,6)	0.80	Metallic
M2	(13,13)	1.73	Metallic

Table S3. Comparison of reported *PF* values for various CNT samples.

	Sample details (original production method)	Dopant	σ (S/m)	S (μV/K)	PF (mW/mK^2)	Reference
Unsorted	Buckypaper (CVD)	N/A (no intentional doping)	3.2×10^5	88	2.48	[13]
	Aligned yarn (CVD)	$FeCl_3$	7.5×10^5	57	2.39	[14]
	Web (CVD)	BV	2.2×10^5	-120	3.10	[15]
	Aligned fiber (eDIPS)	N/A (annealed)	2.9×10^6	68	14	This work
	Film (AD)	OA	5.1×10^4	84	0.36	[16]

Semiconductor-enriched	Film (pulsed LV)		1.1×10^5	70	0.56	
	Film (HiPco)		1.5×10^5	69	0.71	
	Film (Plasma Torch)	BV	1.2×10^5	-79	0.73	
	(6,5) film (HiPco)	N/A (no intentional doping)	6.2×10^3	103	0.066	[7]
Metal-enriched	Film (AD)		4.8×10^4	33	0.052	
	Aligned film (AD)		3.6×10^5	28	0.28	
CNT-filled polymer nanocomposites	PANI/graphene/PANI/DWCNT	N/A (no intentional doping)	1.1×10^5	130	1.83	[17]
	PANI/graphene-PEDOT:PSS/PANI/DWCNT-PEDOT:PSS		1.9×10^5	120	2.71	[18]
	PANI/graphene/PANI/DWCNT		2.2×10^5	118	3.05	[19]

*Abbreviations used; CVD: chemical vapor deposition, eDIPS: enhanced direct injection pyrolytic synthesis, BV: benzyl viologen, AD: arc-discharge, LV: laser vaporization, OA: Triethyloxonium hexachloroantimonate, PANI: polyaniline, and PEDOT:PSS: Poly(3,4ethylenedioxythiophene):poly(styrenesulfonate)

Table S4. Comparison of calculated effective thermal conductivity κ_{eff}, defined as[20] $\kappa_{\text{eff}} = \kappa + \frac{PFT^2}{2\Delta T}$, for representative materials at a ΔT of 1 K.

Materials		T (K)	σ (S/m)	S (μV/K)	PF (mW/mK^2)	κ (W/mK)	κ_{eff} (W/mk)	Ref.
	CNT fiber	300	2.9×10^6	68	14	580*	1,190	This work
Metals	Co	300	1.7×10^7	-30	15	100	780	[21]
	$YbAl_3$	300	2.7×10^6	-77	16	21	740	[22]
	CuNi	400	2.1×10^6	-53	5.8	29	460	[23]
	AgPd	400	3.2×10^6	-40	5.1	36	440	[23]
	$CePd_3$	300	9.1×10^5	92	7.7	10	360	[24]
	Alumel	300	3.4×10^6	-16	0.8	29	70	[25,26]
	Chromel	300	1.4×10^6	26	1.0	17	60	[25,26]
Conventional TE	Bi_2Te_3	300	1.0×10^5	210	4.5	1.2	200	[27]
	$Cu_{0.9}Ni_{0.1}AgSe$	300	5.9×10^5	-85	5.8	4.7	200	[28]
	$Mg_3Bi_{1.25}Sb$	300	9.1×10^4	-210	4.1	1.5	180	[29]

materials	$CsBi_4Te_6$	300	1.0×10^5	105	1.1	0.5	50	[30]

*Thermal conductivity value was taken from Ref. [31]

REFERENCES

1. Headrick, R. J. *et al.* Structure–Property Relations in Carbon Nanotube Fibers by Downscaling Solution Processing. *Adv. Mater.* **30**, 1704482 (2018).
2. Weisman, R. B. & Bachilo, S. M. Dependence of optical transition energies on structure for single-walled carbon nanotubes in aqueous suspension: An empirical Kataura plot. *Nano Lett.* **3**, 1235–1238 (2003).
3. Weisman, B. R. & Kono, J. *Optical Properties of Carbon Nanotubes: A Volume Dedicated to the Memory of Professor Mildred Dresselhaus*. (World Scientific Publishing, 2019).
4. Yanagi, K. *et al.* Intersubband plasmons in the quantum limit in gated and aligned carbon nanotubes. *Nat. Commun.* **9**, 1121 (2018).
5. Koskinen, P. & Mäkinen, V. Density-functional tight-binding for beginners. *Comput. Mater. Sci.* **47**, 237–253 (2009).
6. Stokbro, K. *et al.* Semiempirical model for nanoscale device simulations. *Phys. Rev. B* **82**, 075420 (2010).
7. Ichinose, Y. *et al.* Solving the Thermoelectric Trade-Off Problem with Metallic Carbon Nanotubes. *Nano Lett.* **19**, 7370–7376 (2019).
8. Hayashi, D. *et al.* Thermoelectric properties of single-wall carbon nanotube networks. *Jpn. J. Appl. Phys.* **58**, 075003 (2019).

9. Romero, H. E., Sumanasekera, G. U., Mahan, G. D. & Eklund, P. C. Thermoelectric power of single-walled carbon nanotube films. *Phys. Rev. B* **65**, 1–6 (2002).

10. Esfarjani, K. & Zebarjadi, M. Thermoelectric properties of a nanocontact made of two-capped single-wall carbon nanotubes calculated within the tight-binding approximation. *Phys. Rev. B* **73**, 085406 (2006).

11. Hayashi, D. *et al.* Temperature dependence of the Seebeck coefficient for mixed semiconducting and metallic single-wall carbon nanotube bundles. *Appl. Phys. Express* **13**, 015001 (2020).

12. Nakai, Y. *et al.* Giant Seebeck coefficient in semiconducting single-wall carbon nanotube film Thermoelectric properties of single-wall carbon nanotube films: Effects of diameter and wet environment. *Appl. Phys. Express* **7**, 025103 (2014).

13. Zhou, W. Bin *et al.* Ultrahigh-power-factor carbon nanotubes and an ingenious strategy for thermoelectric performance evaluation. *Small* **12**, 3407–3414 (2016).

14. Choi, J. *et al.* Flexible and Robust Thermoelectric Generators Based on All-Carbon Nanotube Yarn without Metal Electrodes. *ACS Nano* **11**, 7608–7614 (2017).

15. An, C. J., Kang, Y. H., Song, H., Jeong, Y. & Cho, S. Y. High-performance flexible thermoelectric generator by control of electronic structure of directly spun carbon nanotube webs with various molecular dopants. *J. Mater. Chem. A* **5**, 15631–15639 (2017).

16. Macleod, B. A., Stanton, N., Gould, I., Wesenberg, D. & Ihly, R. Large n - and p - type thermoelectric power factors from doped semiconducting single - walled carbon nanotube thin films. *Energy Environ. Sci.* **10**, 2168–2179 (2017).

17. Cho, C. *et al.* Completely organic multilayer thin film with thermoelectric power factor rivaling inorganic tellurides. *Adv. Mater.* **27**, 2996–3001 (2015).

18. Cho, C. *et al.* Outstanding Low Temperature Thermoelectric Power Factor from Completely Organic Thin Films Enabled by Multidimensional Conjugated Nanomaterials. *Adv. Energy Mater.* **6**, 1502168 (2016).

19. Cho, C. *et al.* Organic thermoelectric thin films with large p-type and n-type power factor. *J. Mater. Sci.* **56**, 4291–4304 (2021).

20. Adams, M. J., Verosky, M., Zebarjadi, M. & Heremans, J. P. Active Peltier Coolers Based on Correlated and Magnon-Drag Metals. *Phys. Rev. Appl.* **11**, 054008 (2019).

21. Watzman, S. J. *et al.* Magnon-drag thermopower and Nernst coefficient in Fe, Co, and Ni. *Phys. Rev. B* **94**, 144407 (2016).

22. Rowe, D. M., Kuznetsov, V. L., Kuznetsova, L. A. & Min, G. Electrical and thermal transport properties of intermediate-valence YbAl 3. *J. Phys. D Appl. Phys* **35**, 2183–2186 (2006).

23. Yarbrough, D. W. & Graves, R. S. Transport properties of concentrated Ag-Pd and Cu-Ni alloys from 300-1000 K. in *Thermal Conductivity 16* 319–324 (1983).

24. Boona, S. R. & Morelli, D. T. Enhanced thermoelectric properties of CePd 3-xPt x. *Appl. Phys. Lett.* **101**, 101909 (2012).

25. Sundqvist, B. Thermal diffusivity and thermal conductivity of Chromel, Alumel, and Constantan in the range 100-450 K. *J. Appl. Phys.* **72**, 539–545 (1992).

26. Pollock, D. D. *Thermocouples: theory and properties*. (CRC Press, 1991).

27. Poudel, B. *et al.* High-Thermoelectric Performance of Nanostructured Bismuth Antimony Telluride Bulk Alloys. *Science (80-.).* **320**, 634–638 (2008).

28. Ishiwata, S. *et al.* Extremely high electron mobility in a phonon-glass semimetal. *Nat. Mater.* **12**, 512–517 (2013).

29. Pan, Y. *et al.* Mg3(Bi,Sb)2single crystals towards high thermoelectric performance. *Energy Environ. Sci.* **13**, 1717–1724 (2020).

30. Chung, D.-Y. *et al.* CsBi4Te6: A high-performance thermoelectric material for low-temperature applications. *Science (80-.).* **287**, 1024–1027 (2000).

31. Behabtu, N. *et al.* Strong, Light, Multifunctional Fibers of Carbon Nanotubes with Ultrahigh Conductivity. *Science (80-.).* **339**, 182 (2013).